



Deposited via The University of Sheffield.

White Rose Research Online URL for this paper:

<https://eprints.whiterose.ac.uk/id/eprint/217010/>

Version: Published Version

---

**Article:**

Chaithanya, K.V.S., Ardaševa, A., Meacock, O.J. et al. (2024) Transport of topological defects in a biphasic mixture of active and passive nematic fluids. *Communications Physics*, 7 (1). 302. ISSN: 2399-3650

<https://doi.org/10.1038/s42005-024-01792-6>

---

**Reuse**

This article is distributed under the terms of the Creative Commons Attribution-NonCommercial-NoDerivs (CC BY-NC-ND) licence. This licence only allows you to download this work and share it with others as long as you credit the authors, but you can't change the article in any way or use it commercially. More information and the full terms of the licence here: <https://creativecommons.org/licenses/>

**Takedown**

If you consider content in White Rose Research Online to be in breach of UK law, please notify us by emailing [eprints@whiterose.ac.uk](mailto:eprints@whiterose.ac.uk) including the URL of the record and the reason for the withdrawal request.

<https://doi.org/10.1038/s42005-024-01792-6>

# Transport of topological defects in a biphasic mixture of active and passive nematic fluids

Check for updates

K. V. S. Chaithanya <sup>1</sup>, Aleksandra Ardaševa <sup>2</sup>, Oliver J. Meacock <sup>3</sup>, William M. Durham <sup>4</sup>,  
Sumesh P. Thampi <sup>5</sup> & Amin Doostmohammadi <sup>2</sup>

Collectively moving cellular systems often contain a proportion of dead cells or non-motile genotypes. When mixed, nematically aligning motile and non-motile agents are known to segregate spontaneously. However, the role that topological defects and active stresses play in shaping the distribution of the two phases remains unresolved. In this study, we investigate the behaviour of a two-dimensional binary mixture of active and passive nematic fluids to understand how topological defects are transported between the two phases and, ultimately, how this leads to the segregation of topological charges. When the activity of the motile phase is large, and the tension at the interface of motile and non-motile phases is weak, we find that the active phase tends to accumulate  $+1/2$  defects and expel  $-1/2$  defects so that the motile phase develops a net positive charge. Conversely, when the activity of the motile phase is comparatively small and interfacial tension is strong, the opposite occurs so that the active phase develops a net negative charge. We then use these simulations to develop a physical intuition of the underlying processes that drive the charge segregation. Lastly, we quantify the sensitivity of this process on the other model parameters, by exploring the effect that anchoring strength, orientational elasticity, friction, and volume fraction of the motile phase have on topological charge segregation. As  $+1/2$  and  $-1/2$  defects have very different effects on interface morphology and fluid transport, this study offers new insights into the spontaneous pattern formation that occurs when motile and non-motile cells interact.

Collective motility is observed in a wide diversity of systems where cells live in close proximity to each other, ranging from microbial communities in the environment to tumors within the human body. However, such collectively moving systems often contain a significant fraction of non-motile cells, commonly due to the loss of motility in some members or their inability to acquire it<sup>1–3</sup>. The interactions between motile and non-motile cells are crucial in shaping the dynamics, stability, and functionality of these systems, thus playing a key role in these microecosystems<sup>4,5</sup>. For instance, in biofilms, bacteria can use motility-based segregation to evade exposure to antibiotics<sup>6,7</sup>. Similarly, cancer tumors present a varied composition, comprising both active and necrotic cells that vary in their motility<sup>8,9</sup>. Understanding these interactions is crucial for unraveling the mechanisms driving tumor invasion and bacterial

infection, including their treatment and resistance to therapies. Despite their prevalence, relatively few studies have examined systems with both motile and non-motile phases, limiting our understanding of how these interact with one another. Here, we investigate the behavior of a binary mixture of active and passive fluids using a biphasic active nematic framework to understand the interactions between motile and non-motile phases.

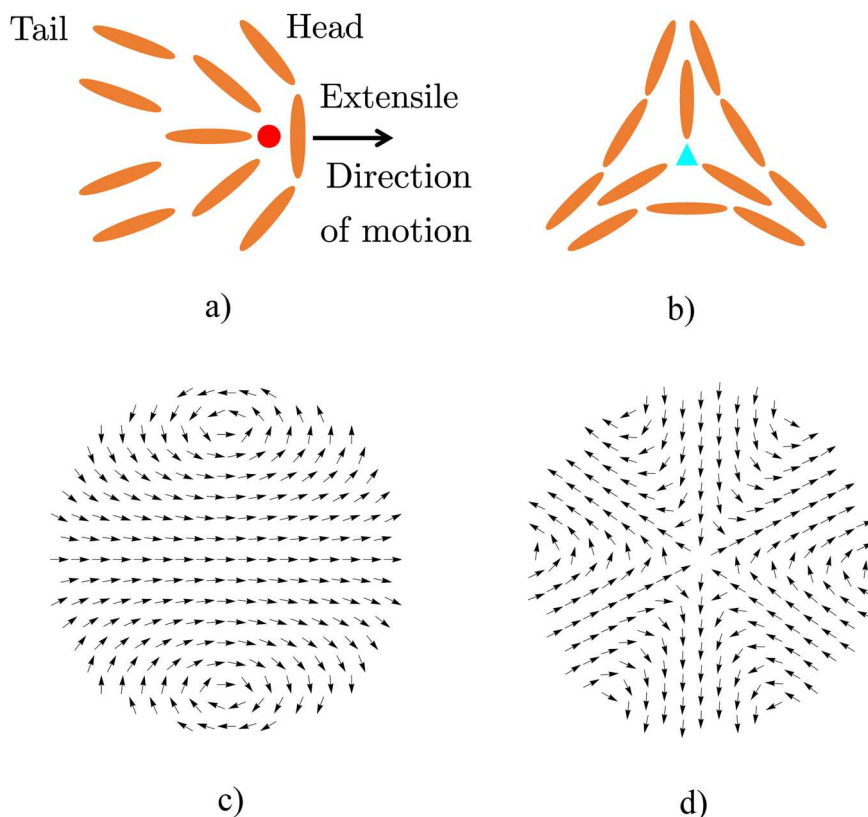
The constituents of many active systems, such as eukaryotic cells<sup>10,11</sup>, bacterial colonies<sup>12</sup>, microtubule-kinesin mixtures<sup>13</sup>, and active filaments<sup>14</sup> have nematic symmetry. Thus, active nematic theories have been instrumental in understanding the large-scale flow patterns and coherent motion observed in these systems<sup>15,16</sup>. One of the remarkable features of two-dimensional active nematics is the formation of half-integer ( $\pm 1/2$ )

<sup>1</sup>School of Life Sciences, University of Dundee, Dundee, United Kingdom. <sup>2</sup>Niels Bohr Institute, University of Copenhagen, Blegdamsvej 17, Copenhagen, Denmark.

<sup>3</sup>Department of Fundamental Microbiology, University of Lausanne, Lausanne, Switzerland. <sup>4</sup>Department of Physics and Astronomy, University of Sheffield, Sheffield, United Kingdom. <sup>5</sup>Department of Chemical Engineering, Indian Institute of Technology Madras, Chennai, India. e-mail: [sumesh@iitm.ac.in](mailto:sumesh@iitm.ac.in);

[doostmohammadi@nbi.ku.dk](mailto:doostmohammadi@nbi.ku.dk)

**Fig. 1 | Topological defects.** Schematic illustrating the director texture surrounding (a)  $+1/2$  and (b)  $-1/2$  topological defects observed in active nematic liquid crystals. The red circle denotes the core of the  $+1/2$  defect, while the core of the  $-1/2$  defect is represented by a cyan triangle. Panels c and d illustrate the corresponding velocity field surrounding the  $+1/2$  and  $-1/2$  defects for extensile activity, respectively, computed using analytical expressions from ref. 77.



topological defects<sup>17</sup>. These are regions of broken orientational order, as shown in Fig. 1.

Recently, there has been a growing interest in understanding the role of topological defects on the dynamics of a binary mixture of active nematic materials with different levels of activity. For instance, Meacock et al.<sup>18</sup> demonstrated how bacteria that move at different rates compete with one another when mixed together in colonies. Fast-moving cells can become trapped vertically in rosettes formed due to the merger of two  $+1/2$  defects, which then allows slower-moving cells to outcompete them. Similarly, Zhang et al.<sup>19</sup> investigated defect-mediated morphogenesis of initially flat active-active interfaces using biphasic nematic theory and experiments based on Mardin-Darby canine kidney (MDCK) and mouse myoblast (C2C12) cells. They identified activity-mediated defect-interface interactions and studied the morphodynamics of an initially flat active-active interface, demonstrating the activity-dependent segregation of topological defects in a binary mixture of two active fluids. The passive liquid crystalline environment can also be pre-patterned to guide active nematic motion<sup>20,21</sup>. On the other hand, spatially patterned activity has been shown to influence the dynamics of topological defects<sup>22,23</sup> and drive their segregation<sup>24,25</sup>. Moreover,  $+1/2$  defects have been shown to induce apoptotic cell extrusion in MDCK cell layers<sup>10</sup>, and multilayer formation in soil bacteria<sup>26</sup>. In contrast,  $-1/2$  defects contribute to hole formation in epithelial cell layers<sup>26,27</sup>. A few studies have probed the phase-separation of a binary mixture of active-isotropic fluids<sup>28,29</sup> and the dynamics of active-isotropic fluid interfaces<sup>30–34</sup>. These studies highlight the role of activity and nematic stresses on microphase separation, active anchoring at the fluid-fluid interface, and spatial distribution of topological defects. Furthermore, the origin of large-scale tissue flows during gastrulation in embryos<sup>35</sup> and in cellular aggregates<sup>36–38</sup> have been modeled as an effective tissue interfacial tension<sup>39,40</sup>, analogous to the interfacial tension observed at fluid-fluid interfaces. Differential adhesion, which occurs when different cell types adhere to one another with different affinities, results in this effective interfacial tension. This process is thought to play a crucial role in tissue morphogenesis and patterning by organizing cells into distinct patterns and structures during

development<sup>41–43</sup>. Nevertheless, the intricate interplay between the forces of activity and interfacial tension in systems with two cell types remains largely unexplored.

In this study, we employ the biphasic nematic framework to investigate the defect transport and the segregation of topological charges within a binary mixture of active-passive nematic fluids. We demonstrate that the charge of the active fluid can be tuned via the interplay between activity and interfacial tension. For high activities and low interfacial tension, we find the active fluid becomes positively charged due to the accumulation of active nematic within the cores of  $+1/2$  defects and its depletion from  $-1/2$  defect cores, a phenomenon that is consistent with experimental findings in monolayers composed of a single type of cells like epithelial cell layers<sup>44</sup>, neural progenitor cells<sup>26</sup>, and soil bacteria<sup>27</sup>. For larger interfacial tension and lower activity, the  $+1/2$  defects are expelled from the active nematic, leading to a negatively charged active nematic and a positively charged passive nematic. Further, we establish the correlation between charge segregation and interface morphology. By systematically varying activity and interfacial tension strengths, we construct a phase diagram illustrating the net topological charge of the active nematic to elucidate the intricate interplay between the morphodynamics of interfaces and the transport of defects across these interfaces. Moreover, we demonstrate distinct impacts of the orientational elasticity, anchoring strength, isotropic friction, and the initial concentration of the active fluid on charge segregation. The dependence of the charge segregation on these parameters is shown to align with their impact on the activity and number of topological defects.

## Methods

We extend the two-dimensional lyotropic model, presented by Blow et al.<sup>30</sup>, to account for a biphasic fluid with interfacial tension. The two fluids are distinguished by a scalar order parameter,  $\phi$ , a measure of the relative concentration of each fluid. The nematic order in both fluids is described by a symmetric traceless tensor,  $Q_{\alpha\beta} = S(2n_{\alpha}n_{\beta} - \delta_{\alpha\beta})$ , where  $\mathbf{n}$  describes the director alignment and  $S$  is the magnitude of the nematic order.

The energy density of the system is given by:

$$\mathcal{F} = \int \left[ \frac{A}{2} \phi^2 (1 - \phi)^2 + \frac{1}{2} K (\partial_\gamma \phi) (\partial_\gamma \phi) + \frac{1}{2} C \left( S^2 - \frac{1}{2} Q_{\alpha\beta} Q_{\alpha\beta} \right)^2 + \frac{1}{2} L \partial_\gamma Q_{\alpha\beta} \partial_\gamma Q_{\alpha\beta} - \mu_l \phi \right] d^2 \mathbf{r}, \quad (1)$$

where  $A$ ,  $C$ ,  $K$ , and  $L$  are positive constants. The first term represents a double-well potential with minima at  $\phi = 0$  (passive fluid) and  $1$  (active fluid). The second term is the mixing term that penalizes the gradients in  $\phi$ . These two terms describe the phase separation of two fluids. The interfacial tension between the two fluids is given by  $\gamma = \sqrt{AK}/6^{45}$ . The third term promotes nematic ordering, while the fourth term accounts for the nematic elasticity in the liquid crystalline energy of both fluids. Here  $\mu_l$  is a Lagrange multiplier that conserves the integrated value of  $\phi$ , and  $\mathbf{r}$  is the position vector. From here onward, we use Greek indices to represent Cartesian components, and repeated indices imply summation.

The order parameters,  $\phi$  and  $\mathbf{Q}$ , evolve according to the advection-diffusion equations:

$$\partial_t \phi + \nabla \cdot (\mathbf{u} \phi) = \Gamma_\phi \nabla^2 \mu, \quad (2)$$

$$(\partial_t + \mathbf{u} \cdot \nabla) \mathbf{Q} - \mathbf{R} = \Gamma_Q \mathbf{H}, \quad (3)$$

where  $\mathbf{u}$  is the velocity field,  $\Gamma_\phi$  is the interface mobility parameter, which describes the rate at which  $\phi$  responds to the gradients in the chemical potential,  $\mu = \frac{\partial \mathcal{F}}{\partial \phi}$ . Similarly,  $\Gamma_Q$  is the rotational diffusivity and  $\mathbf{H}$  is the molecular field, defined as:

$$\mathbf{H} = - \left( \frac{\partial \mathcal{F}}{\partial \mathbf{Q}} - (\mathbf{I}/2) \text{Tr} \frac{\partial \mathcal{F}}{\partial \mathbf{Q}} \right), \quad (4)$$

where  $\mathbf{I}$  is the identity matrix and  $\text{Tr}$  denotes the tensorial trace. Unlike the order parameter,  $\phi$ , which only gets advected by the flow, the nematic constituents can rotate in response to the flow gradients. This is accounted by the co-rotation term:

$$R_{ij} = (\xi D_{ik} + \Omega_{ik}) \left( Q_{kj} + \frac{\delta_{kj}}{2} \right) + \left( Q_{ik} + \frac{\delta_{ik}}{2} \right) (\xi D_{kj} - \Omega_{kj}) - 2\xi \left( Q_{ij} + \frac{\delta_{ij}}{2} \right) Q_{kl} W_{lk}, \quad (5)$$

where  $D_{ij} = (\partial_j u_i + \partial_i u_j)/2$  and  $\Omega_{ij} = (\partial_j u_i - \partial_i u_j)/2$  are the symmetric and anti-symmetric parts, respectively, of the velocity gradient tensor,  $W_{ij} = \partial_j u_i$ .

**Table 1 | Values of the parameters used in the biphasic model**

Parameter	Numerical value
Kinematic viscosity, $\nu = \eta/\rho$	0.167
Rotational diffusivity, $\Gamma_Q$	0.1
Mobility, $\Gamma_\phi$	0.1
Tumbling parameter, $\lambda$	0.3
Surface tension, $\gamma$	0.015–0.060
Parameter in free energy (Eq. (1)), $C$	0.5
orientational elasticity, $L$	0.00–0.25
Activity, $\zeta$	0.00–0.30
Friction coefficient, $\chi_0$	0.0–10

The parameter  $\xi$  quantifies the response of the director to the shear flow, and is related to the flow alignment parameter,  $\lambda = \xi/(2S)$ .

The fluid velocity evolves according to the Navier–Stokes equations:

$$\begin{aligned} \nabla \cdot \mathbf{u} &= 0, \\ \rho (\partial_t + \mathbf{u} \cdot \nabla) \mathbf{u} &= \nabla \cdot \boldsymbol{\sigma} - \chi \mathbf{u}, \end{aligned} \quad (6)$$

where  $\rho$  denotes the fluid density,  $\boldsymbol{\sigma} = \boldsymbol{\sigma}_{\text{passive}} + \boldsymbol{\sigma}_{\text{active}}$  represents the stress tensor encompassing both active and passive contributions, and  $\chi$  is the friction coefficient<sup>46</sup>.

The passive contributions to stress in both fluids are given by,  $\boldsymbol{\sigma}_{\text{passive}} = \boldsymbol{\sigma}_{\text{viscous}} + \boldsymbol{\sigma}_{\text{capillary}} + \boldsymbol{\sigma}_{\text{elastic}}$

$$\boldsymbol{\sigma}_{\text{viscous}} = 2\eta \mathbf{D}, \quad (7)$$

$$\begin{aligned} \boldsymbol{\sigma}_{\text{capillary}} &= (\mathcal{F} - \mu \phi) \mathbf{I} - \nabla \phi \left( \frac{\partial \mathcal{F}}{\partial (\nabla \phi)} \right) \\ &+ \nabla \phi \left( \frac{\partial \mathcal{F}}{\partial (\nabla^2 \phi)} \right) - \nabla \nabla \phi \left( \frac{\partial \mathcal{F}}{\partial (\nabla^2 \phi)} \right), \end{aligned} \quad (8)$$

$$\begin{aligned} \boldsymbol{\sigma}_{\text{elastic}} &= -p \mathbf{I} - \xi (\mathbf{H}(\mathbf{Q} + \mathbf{I}/2) + (\mathbf{Q} + \mathbf{I}/2)\mathbf{H} \\ &- 2(\mathbf{Q} + \mathbf{I}/2) \text{Tr}(\mathbf{QH}) + \mathbf{QH} \\ &- \mathbf{HQ} - \nabla \mathbf{Q} \left( \frac{\partial \mathcal{F}}{\partial (\nabla \mathbf{Q})} \right), \end{aligned} \quad (9)$$

where  $\rho$  is the fluid density,  $\eta$  is the fluid viscosity,  $p$  is the bulk pressure.

The active contribution to the stress in the active fluid ( $\phi = 1.0$ ) is given by,

$$\boldsymbol{\sigma}_{\text{active}} = -\zeta \mathbf{Q}, \quad (10)$$

where  $\zeta$  represents the activity coefficient. A positive  $\zeta$  corresponds to an extensile material, while a negative  $\zeta$  corresponds to a contractile material.

The coupled equations for fluid velocity (Eq. (6)), the nematic (Eq. (3)) and phase-field order parameters (Eq. (2)) are solved using hybrid lattice-Boltzmann method<sup>47,48</sup> with periodic boundary conditions on square domain  $L \times L$  of size  $L = 500$ . The frictional force  $-\chi \mathbf{u}$  is incorporated as a force density in the lattice Boltzmann scheme. The spatial and temporal resolutions are chosen as unity. The parameters used in simulations are listed in Table 1. Simulations are initialized with a quiescent velocity field ( $\mathbf{u} = 0$ ), and the phase-field value,  $\phi(t = 0) = 0.50$ , indicating a mixture with equal volume fraction of active fluid,  $\phi_a = \phi(t = 0)$ , and passive fluid,  $\phi_p = 1 - \phi(t = 0)$ . Additionally, the nematic director field is initialized close to the uniformly oriented state,  $\mathbf{n} = \mathbf{e}_x$ , using a random seed.

To vary the surface tension  $\gamma = \sqrt{AK}/6$ , the parameter  $A$  is fixed at 0.5, while  $K$  is varied over the range 0.016–0.260. The results shown represent an average over three distinct simulations, each initialized with a different random seed that prescribes the random distribution of the director field,  $\mathbf{n}$ .

## Results and discussion

### Temporal dynamics

**Phase segregation.** We start by looking at the temporal evolution of the active-passive phases, as depicted in Fig. 2. Initially, the system is in a fully mixed state with  $\phi = 0.50$ , and the director is nematically aligned, albeit with slight fluctuations (Fig. 2a). The double-well potential of the phase field variable  $\phi$  drives the phase separation process, promoting the formation of distinct active and passive phases characterized by  $\phi = 1.0$  and  $\phi = 0.0$ , respectively (Fig. 2b). Simultaneously, the interfacial tension acts to minimize the length of the interface between these phases, facilitating the demixing process. In contrast to mixtures of passive isotropic fluids which segregate and stabilize into a minimum energy equilibrium configuration<sup>49,50</sup>, in the active nematic system, domains of active and passive fluids display a dynamic behavior; the domains continuously break up and reform. Additionally, the presence of extensile active flows causes these domains to elongate parallel to

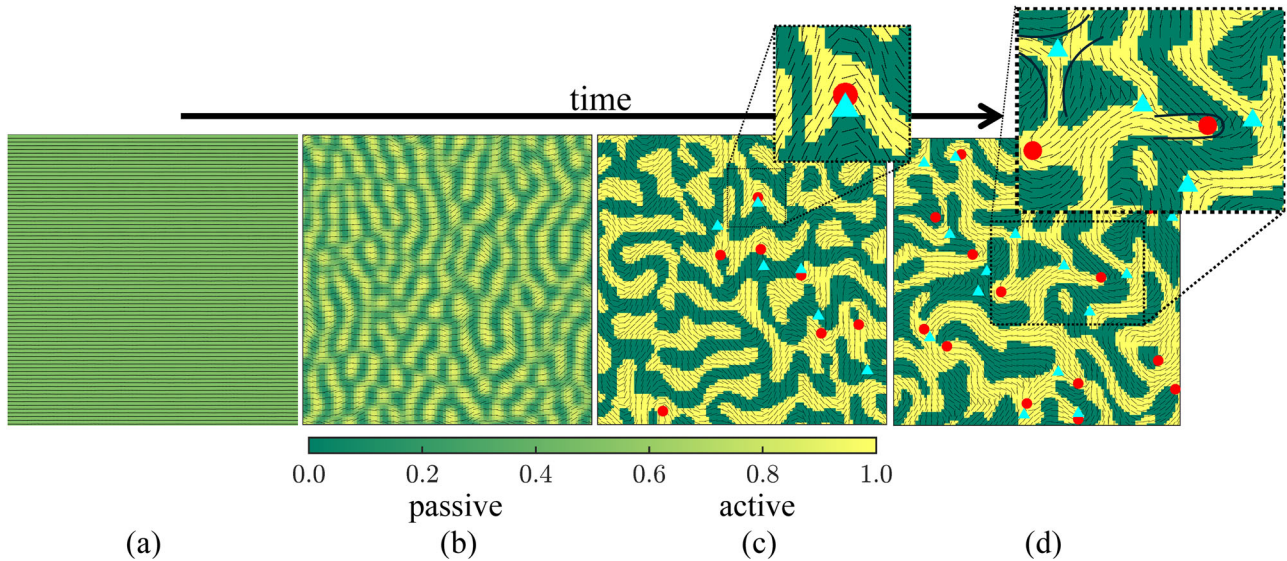


**Fig. 2 | Phase segregation.** The time evolution of the phase field variable ( $\phi$ ) for  $\zeta = 0.15$  and  $K = 0.05$ , with overlaid director field (black lines) and topological defects ( $+1/2$  depicted as red circles,  $-1/2$  as cyan triangles). The snapshots correspond to time instances: **a**  $t = 0$ , **b**  $t = 900$ , **c**  $t = 1800$ , and **d**  $t = 25000$  simulation steps. An area

of  $100 \times 100$  within a larger domain sized  $500 \times 500$  is shown for clarity. The zoomed-in region in **c** illustrates typical defect pair generation, and **d** shows the fluid-fluid interface morphology around the defects.

the director field<sup>28,30</sup> (Fig. 2d). While interfacial tension drives the demixing of the active and passive fluids by minimizing the length of the interface between the two fluids, activity drives fluid mixing by elongating the interface between them. This interplay between interfacial tension and activity significantly influences the dynamics and morphology of the phase-separated domains.

Furthermore, the active flows induce local distortions in the nematic order, thereby promoting the formation of half-integer topological defects<sup>30</sup>. As time progresses, we observe the spontaneous emergence of these defects (Fig. 2c). Subsequently, these defects traverse across the fluid-fluid interface, enabling a continuous exchange of topological defects between the passive and active fluids (Fig. 2d). This behavior contrasts with that of a single nematic fluid or a nematic-isotropic fluid mixture, where defects typically remain localized within the active fluid<sup>30</sup>.

Additionally, Fig. 2d illustrates the morphology of the fluid-fluid interface near topological defects. The director field associated with a  $+1/2$  defect promotes the formation of a comet-shaped interface, while a  $-1/2$  defect induces a trefoil-shaped interface. This occurs because the extensile active flows elongate the fluid domains parallel to the director field (Supplementary Fig. 1). Moreover, Fig. 2d highlights the effect of effective anchoring, where the director field aligns parallel to the fluid-fluid interface, as observed in a nematic-isotropic mixture<sup>30</sup>.

**Charge segregation.** In active nematic fluids, half-integer defects ( $\pm 1/2$ ) are always generated in pairs, maintaining the overall charge neutrality of the system<sup>15</sup>. In contrast, in the present case, the defects can traverse between the active and passive fluids; their exchange can be uneven, leading to disruptions in the charge neutrality within each phase. Consequently, one type of defect (either  $+1/2$  or  $-1/2$ ) may predominate in a given fluid, resulting in a net positive or negative charge. This phenomenon is referred to as the *charge segregation*<sup>19</sup>.

We quantify the charge segregation in terms of the average charge of the active fluid defined as,

$$c = \frac{\phi_a q_a}{N}. \tag{11}$$

Here,  $q_a$  is the net charge of the active fluid, defined as the sum of positive and negative topological charges of defects present in the active fluid, and  $N = \phi_a N_a + \phi_p N_p$  denotes the total number of defects in the

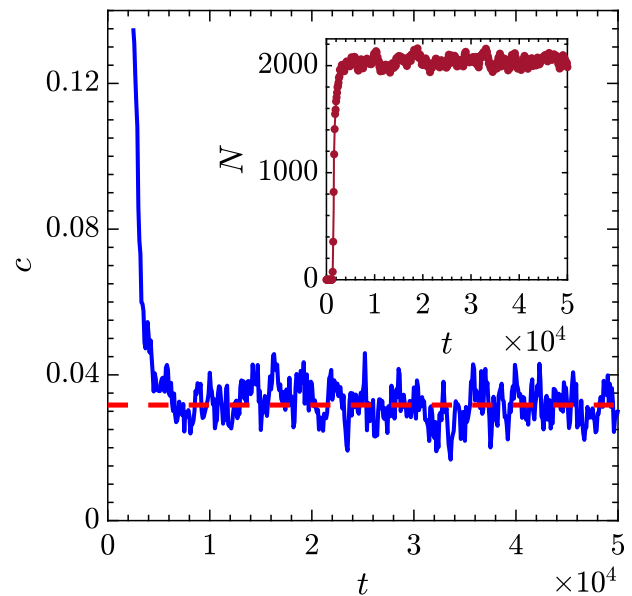


**Fig. 3 | Charge segregation.** The time evolution of the charge of the active fluid for  $\zeta = 0.15$  and  $K = 0.05$ . The red dashed line indicates the average charge, corresponding to a dynamical steady state. Inset shows the temporal evolution of the total number of defects ( $N$ ) in the system.

system, encompassing both the number of defects in active ( $N_a$ ) and passive ( $N_p$ ) fluids. When  $+1/2$  defects outnumber  $-1/2$  defects in the active fluid,  $c$  assumes a positive value ( $c > 0$ ), signifying a positively charged active fluid. Conversely, if  $-1/2$  defects prevail in the active fluid compared to  $+1/2$  defects,  $c$  takes a negative value ( $c < 0$ ), indicating a negatively charged active fluid. Furthermore, the charge of the passive fluid is complementary such that  $c > 0$  denotes a negatively charged passive fluid, while  $c < 0$  implies a positively charged passive fluid.

Figure 3 illustrates the temporal evolution of (i) the total number of defects in the system (inset of Fig. 3) and (ii) the charge of the active fluid ( $c$ ) for  $\zeta = 0.15$  and  $K = 0.05$ . Initially, the total number of defects increases rapidly, eventually stabilizing into a dynamic steady state, with number of

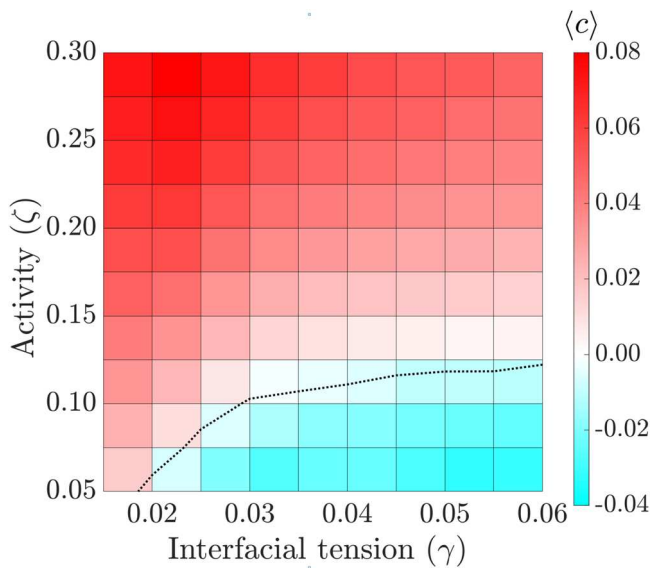


**Fig. 4 | Sensitivity of active fluids’ charge to activity and interfacial tension.** Phase diagram depicting the dependence of average charge of active fluid on activity ( $\zeta$ ) and interfacial tension ( $\gamma$ ) for  $L = 0.06$ . The black dotted line marks the region where the average charge ( $\langle c \rangle$ ) equals zero, indicating a change in the sign of the active fluids’ charge.

defects fluctuating about a mean value. On the other hand, the charge of the active fluid starts at a large value and gradually decreases until it reaches a dynamic steady state. The charge of the active fluid fluctuates around this mean positive value indicated by the red dashed line in Fig. 3 indicating a larger number of  $+1/2$  defects compared to  $-1/2$  defects in the active fluid. This phenomenon occurs because defect pairs are usually generated in such a way that the  $+1/2$  defect forms within the bulk of the active fluid and is oriented away from the interface, while the  $-1/2$  defect forms relatively near the interface. This configuration arises because  $+1/2$  defects induce a bend in the director field, which is more compatible with surfaces with large mean curvature, while  $-1/2$  defects induce splay deformations that fit better with surfaces with small mean curvature<sup>51,52</sup>. As defects are continuously exchanged between the active and passive fluids, the charge of the active fluid stabilizes, fluctuating around a mean value. The fluctuations in the charge suggest that the system reaches a dynamic steady state, marked by the continuous exchange of topological defects between the two fluids. Similarly, the fluctuations in the total number of defects result from the continuous process of defect annihilation and creation. This behavior contrasts with that observed in prepatterned stationary activity gradients with zero curvature<sup>24,25</sup>. In such scenarios,  $+1/2$  defects typically exhibit orientational polarization and tend to accumulate on the passive side of the interface due to weak motility, while  $-1/2$  defects remain within the active fluid. However, in this study, the activity is not prepatterned - instead, the spatiotemporal dynamics of activity are coupled to the evolution of the phase-field parameter,  $\phi$ .

**Sensitivity of charge segregation to interfacial tension and activity**

To assess the dependence of charge segregation on activity and interfacial tension, we define the time-averaged charge of the active fluid as follows:

$$\langle c \rangle = \frac{1}{T} \sum_{t=t_i}^{t_f} c(t). \tag{12}$$

Here, we calculate the average charge between  $t_i = 3.5 \times 10^4$  and  $t_f = 5 \times 10^4$  in steps of  $\Delta t = 100$ , i.e.,  $T = 150$ . Figure 4 depicts the dependence of the average charge of the active fluid,  $\langle c \rangle$ , on interfacial tension,  $\gamma$ , and

activity,  $\zeta$ . An increase in interfacial tension ( $\gamma$ ) indicates greater adhesion between the two cell types. On the other hand, increasing activity ( $\zeta$ ) corresponds to larger cellular motility.

When interfacial tension is maintained constant, an increase in activity leads to an increase in the charge of the active fluid, eventually transitioning from negative to positive. Conversely, with constant activity, the charge of the active fluid decreases as interfacial tension increases. The plot illustrates that it is not solely due to the activity but rather the interplay between activity and interfacial tension that determines the charge of the active fluid. Specifically, low activity combined with high interfacial tension yields a negatively charged active fluid, while high activity combined with low interfacial tension results in a positive charge. Additionally, the critical activity at which the charge changes sign from negative to positive depends on the interfacial tension, as indicated by the black dotted curve in Fig. 4. The critical activity for the charge reversal increases with an increase in interfacial tension.

**Defect migration across phases leads to charge segregation**

To resolve the mechanisms underlying charge segregation, we explore various pathways of defect transport between the two fluids. Specifically, we look at the interactions between the  $\pm 1/2$  defects and the fluid-fluid interface.

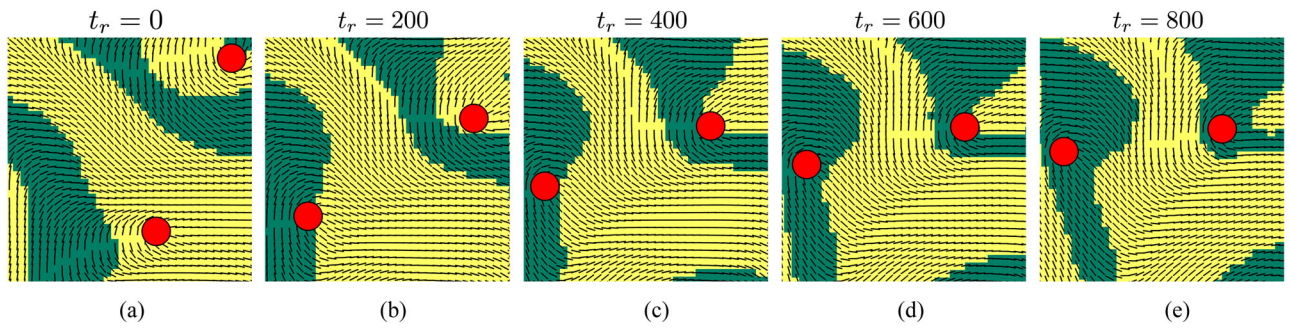
**Transport of  $+1/2$  defects.** First, we focus on the behavior of  $+1/2$  defects near a fluid-fluid interface, depicted in the Fig. 5. The first row (Fig. 5a–e) shows a representative scenario, which is prevalent when interfacial tension is large and activity is small. The  $+1/2$  defects are generated in the bulk of the active fluid (Fig. 5a) and migrate toward the fluid-fluid interface due to their inherent motility (Fig. 5a, c). The director field around a  $+1/2$  defect locally deforms the interface to a comet-like shape (Fig. 2d). Simultaneously, the associated source-sink velocity field (Fig. 1c) drives the interface in the same direction as the defect, forming an active streak. These dynamics are also evident in Supplementary Fig. 1a, which depicts the trajectories of a line of tracers in the analytical velocity field shown in Fig. 1. Interfacial tension, in turn, resists the deformation of the interface. Therefore, when interfacial tension dominates the activity, the elongation of the streak is limited, and  $+1/2$  defects migrate towards the tip of the active streak and eventually exit the active fluid and enter the passive fluid<sup>51</sup>, as shown in Fig. 5d, e.

On the other hand, the second row of Fig. 5 illustrates the scenario in which activity dominates over interfacial tension. Under these conditions, there is minimal resistance to streak deformation and mobility. Consequently, the  $+1/2$  defects tunnel through the active streak (Fig. 5f, g), effectively advecting the interface and merging with another active streak (Fig. 5h). Subsequently, the  $+1/2$  defect and the corresponding active streak integrate into another active streak (Fig. 5i–j). Through this pathway, the  $+1/2$  defects traverse predominantly in the active fluid via the continuous remodeling of fluid phases.

**Transport of  $-1/2$  defects.** Here, we examine the behavior of  $-1/2$  defects near a fluid-fluid interface. Unlike  $+1/2$  defects,  $-1/2$  defects are non-motile and are advected by the fluid as passive tracers. Therefore, their direct impact on interface morphology and charge segregation is limited to when they are located close to the fluid-fluid interface.

When interfacial tension is large and activity is small, the large size of the fluid domains, combined with the weak flow, causes the non-motile  $-1/2$  defects to primarily reside within the bulk of the active fluid. Conversely, when activity dominates over interfacial tension, the  $-1/2$  defects tend to interact more prominently with the fluid-fluid interface. Figure 6 depicts a scenario when  $-1/2$  defect is located close to the fluid-fluid interface. The director field around the  $-1/2$  defects and associated hexapolar velocity field (Fig. 1b, d) locally deforms the interface to a trefoil-like shape (Fig. 6a, b). However, the active fluid eventually drifts away from the defect core along the trefoil axes, driven by extensile activity as depicted in Fig. 6c, d, ultimately entering the passive fluid. These dynamics are also evident in Supplementary

Negatively charged active fluid:  $+1/2$  defects migrating from the active fluid to the passive fluid



Positively charged active fluid:  $+1/2$  defects tunnelling through the active streak

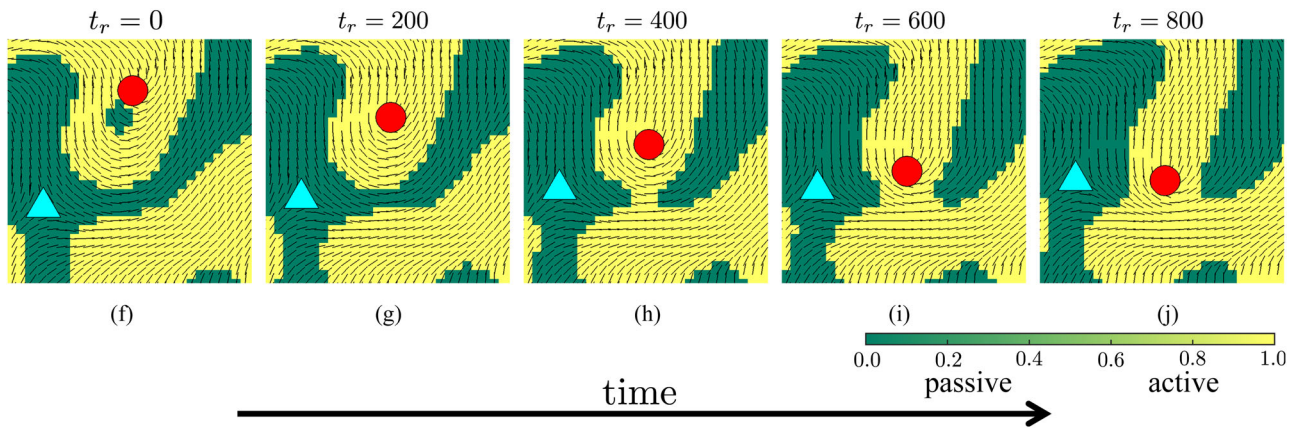


**Fig. 5 | Transport of  $+1/2$  defects in a binary mixture of active-passive nematic fluids.** The  $+1/2$  defect drives the formation of active fluid streaks, countered by interfacial tension. First row **a–e** corresponds to  $\zeta = 0.100$  and  $K = 0.225$ : When interfacial tension dominates over activity,  $+1/2$  defects exit the active fluid and migrate into the passive fluid. Panels **a–e** depict the time evolution of this process.

Second row **f–j** corresponds to  $\zeta = 0.20$  and  $K = 0.10$ : When activity dominates over interfacial tension,  $+1/2$  defects tunnel through the streaks, carrying the streak along, and merge with another active streak.  $t_r$  represents the rescaled simulation time, with its value set to 0 for **a** and **f**.

Positively charged active fluid: fluid advection away from the  $-1/2$  defects

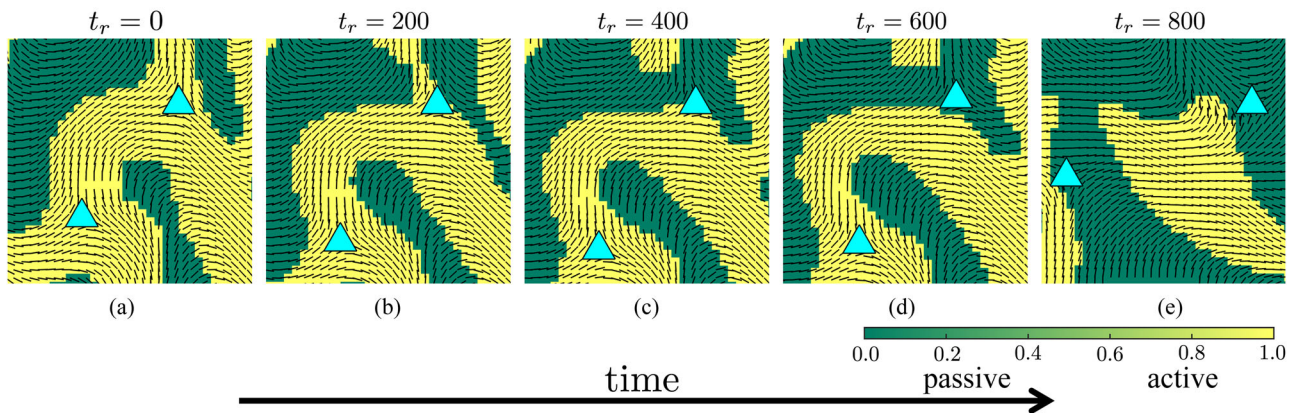


**Fig. 6 | Transport of  $-1/2$  defects in a binary mixture of active-passive nematic fluids.** The active fluid assumes a trefoil shape near the  $-1/2$  defects, and eventually, the fluid is advected away from the defect core. Panels **a–e** depict the time evolution

of this process, with  $t_r$  indicating the rescaled simulation time, with its value set to 0 for **a**, and  $\zeta = 0.20$ ,  $K = 0.10$ .

Fig. 1b, which shows the evolution of an initially circular ring of tracers that advect with the analytical velocity field. The efficacy of the active fluid depletion from the  $-1/2$  defects increases with activity and decreases with interfacial tension.

In summary, increasing activity and decreasing interfacial tension lead to a positively charged active fluid. In these conditions, the  $+1/2$  defects traverse by

joining the active streaks without entering the passive fluid. Meanwhile, the active fluid gradually depletes from  $-1/2$  defects, causing them to enter the passive fluid. Conversely, decreasing activity and increasing interfacial tension yield a negatively charged active fluid. Here,  $+1/2$  defects exit the active fluid due to strong resistance to streak elongation, while  $-1/2$  defects predominantly remain within the active fluid's bulk.

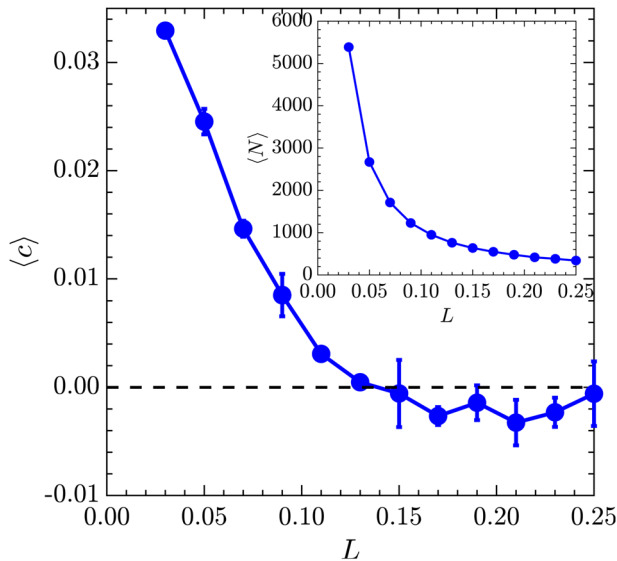


**Fig. 7 | Effect of orientational elasticity,  $L$ .** Variation in the charge of the active fluid to changes in the orientational elasticity for  $\zeta = 0.15$  and  $K = 0.1$ . Inset shows the variation in the number of defects with change in the orientational elasticity. The error bars represent the standard deviation from three distinct simulations, each initialized with a unique random seed defining the random distribution of the director field,  $\mathbf{n}$ .

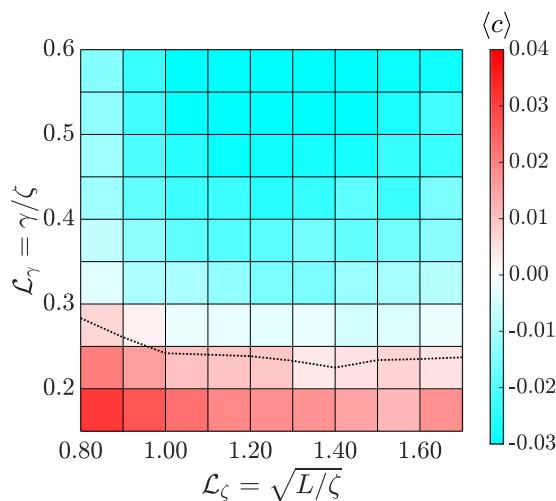


**Fig. 8 | Sensitivity of active fluids' charge to  $\mathcal{L}_\zeta$  and  $\mathcal{L}_\gamma$ .** Phase diagram depicting the dependence of average charge of active fluid on active length scale  $\mathcal{L}_\zeta = \sqrt{L/\zeta}$  and capillary length scale  $\mathcal{L}_\gamma = \gamma/\zeta$ , with  $\zeta = 0.1$ . The black dotted line marks the region where the average charge ( $\langle c \rangle$ ) equals zero, indicating a change in the sign of the active fluid's charge.

**Sensitivity to model parameters**

**Effect of orientational elasticity.** The resistance to the deformation of the nematic structure observed in bacterial colonies and epithelial cell layers depends on the orientational elasticity of the material, characterized by the orientational elasticity constant  $L$  in the model<sup>53</sup>. Figure 7 shows that the charge of the active fluid decreases with an increase in the orientational elasticity. This is attributed to the increasing energy cost of topological distortions as the orientational elasticity increases, leading to a reduction in the total number of defects within the system, as depicted in the inset of Fig. 7. Consequently, it can be inferred that the activity of the fluid effectively decreases with an increase in the orientational elasticity, resulting in a decrease in the charge of the active fluid.

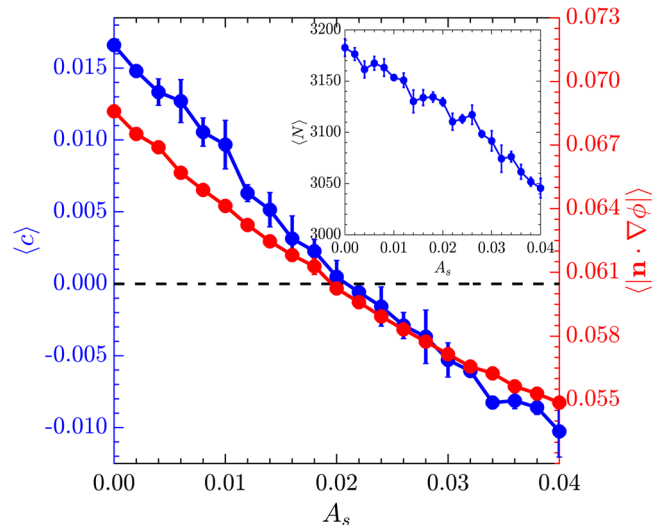


**Fig. 9 | Effect of anchoring strength,  $A_s$ .** Variation in the charge of the active fluid,  $\langle c \rangle$ , (blue curve) and the active anchoring of the director field at the interface,  $\langle |\mathbf{n} \cdot \nabla \phi| \rangle$ , (red curve) to anchoring strength for  $\zeta = 0.15$  and  $K = 0.15$ . Inset shows the variation in the total number of defects ( $\langle N \rangle$ ) in the system with  $A_s$ . The error bars represent the standard deviation from three distinct simulations, each initialized with a unique random seed defining the random distribution of the director field,  $\mathbf{n}$ .

**Active and capillary length scales.** Figures 4 and 7, when considered together, suggest that charge segregation can be understood in terms of the active length scale,  $\mathcal{L}_\zeta = \sqrt{L/\zeta}$ , and the capillary length scale,  $\mathcal{L}_\gamma = \gamma/\zeta$ <sup>34,54,55</sup>. Figure 8 illustrates the charge of the active fluid in the  $\mathcal{L}_\zeta$  and  $\mathcal{L}_\gamma$  phase plane, showing that the charge decreases with an increase in either the active length scale or the capillary length scale. This observation aligns with Figs. 4 and 7, indicating that manipulating these length scales provides a potential strategy for controlling charge segregation in biphasic active nematic systems.

**Effect of anchoring strength.** Next, we examine the impact of interfacial anchoring on charge segregation. Interfacial anchoring has been observed in the bacterial colonies<sup>56</sup> and interacting multicellular monolayers<sup>19</sup>. This anchoring occurs due to the rotation of the nematic director in response to the active force tangential to the interface<sup>30,36</sup>. Consistent with these findings, we observe active anchoring in the biphasic system, where the director field tends to align parallel to the interface. However, the specific orientation of the director field at the interface can be enforced via the free energy term  $\mathcal{F}_a$ <sup>19</sup>,

$$\mathcal{F}_a = \int_A A_s (\partial_\alpha \phi) (\partial_\beta \phi) Q_{\alpha\beta} dA, \tag{13}$$

where  $A_s$  represents the anchoring strength, and  $A_s > 0$  enforces tangential anchoring of the director field at the fluid-fluid interface. Figure 9 illustrates that the charge of the active fluid decreases with increasing anchoring strength (blue curve). To understand the dependence of charge on anchoring strength, we measure the extent of alignment of the director field with the interface in terms of  $\mathbf{n} \cdot \nabla \phi$ . When the director field is aligned parallel to the interface,  $\mathbf{n} \cdot \nabla \phi = 0$ , indicating perfect alignment. Any deviation from zero suggests that the director field is oriented at an angle with the interface, indicating imperfect alignment. As expected, the average value of  $|\mathbf{n} \cdot \nabla \phi|$  decreases with an increase in anchoring strength, indicating a greater alignment of the director field with the interface (Fig. 9 - red curve).

This enhanced alignment, coupled with the elongation of interfaces due to extensile activity, results in a decrease in the number of topological defects, as depicted in the inset of Fig. 9. Therefore, the effect of activity weakens with an increase in anchoring strength, resulting in a decrease in

the charge of the active fluid. Additionally, an increase in anchoring strength increases the resistance to the transport of topological defects across the interface. Given that the passive fluid is predominantly governed by nematic elasticity, the resistance to the  $+1/2$  defects migrating from the passive to active fluid surpasses that in the opposite direction. Consequently, the  $+1/2$  defects tend to remain within the passive fluid, leading to a negatively charged active fluid at high anchoring strength.

On the other hand, when  $A_s < 0$ , the free energy favors homeotropic anchoring, where the director field aligns perpendicular to the interface. This indicates that  $A_s < 0$  corresponds to an incompatibility between the extensile activity and the director field at the interface, making it difficult for  $+1/2$  defects to move across the interface. Consequently, the charge of the active fluid increases as the anchoring strength becomes more negative (Supplementary Fig. 2). This behavior is similar to the observations by Zhang et al.<sup>19</sup> for contractile active nematics with tangential anchoring ( $A_s > 0$ ), since contractile nematics favor homeotropic anchoring at the interface, making tangential anchoring incompatible.

Furthermore, the key difference between the impact of anchoring strength (Fig. 9) and orientational elasticity (Fig. 7) can be observed in the variation in the number of defects in the system. Increasing either anchoring strength or orientational elasticity reduces the number of topological defects, but the decrease is more pronounced with orientational elasticity. As elasticity increases, the number of defects tends to zero, and the system progressively transitions to a defect-free state. Consequently, the net topological charge fluctuates around a mean value of zero. In contrast, as anchoring strength increases, the nematic order only increases in the vicinity of the interface, while the bulk behavior is still governed by passive nematic stresses and active stresses. Therefore, although the number of defects decreases slightly with increased anchoring strength, it does not reach zero. However, the increase in nematic order at the interface resists the transport of topological defects across the interface, resulting in the localization of  $+1/2$  defects in the passive fluid, thereby making the active fluid negatively charged. In summary, the impacts of anchoring strength and orientational elasticity on the system's behavior manifest in distinctly different ways.

**Effect of isotropic friction.** The dynamics of cell colonies are influenced by the interactions between cells and the substrate, quantified in the model as the frictional force,  $-\chi\mathbf{u}$ <sup>56</sup>. These interactions play a crucial role in governing the motion and spatial organization within the cell colonies<sup>57</sup>. Figure 10 plots the charge of the active fluid as a function of the friction coefficient. The charge exhibits a non-monotonic variation with the friction coefficient, initially increasing before subsequently decreasing. This behavior can be attributed to the corresponding variation in the total number of defects within the system, as depicted in the inset of Fig. 10. Such behavior mirrors that observed in a single nematic system<sup>46</sup>, where the number of defects initially increases with friction due to an increase in the number of walls – lines of high distortion separated by nematic region – that decay into defects. However, at higher levels of frictional damping, there is not enough energy available to create defects, resulting in a subsequent decrease in their number.

This behavior can also be analyzed in terms of hydrodynamic screening ( $\mathcal{L}_\chi = \sqrt{\eta/\zeta}$ ) and active length scales<sup>15,46,58</sup> (Supplementary Fig. 3). When the active length scale ( $\mathcal{L}_\zeta$ ) is smaller than the hydrodynamic screening length ( $\mathcal{L}_\chi$ ), hydrodynamic interactions dominate. In this regime, distortions in the nematic director field act as sources of flow, leading to an increase in the number of walls and, consequently, defects. With a weak but finite value of friction, these distortions and the associated flow become more pronounced, promoting the creation of defects. However, as friction continues to increase and the hydrodynamic screening length scale decreases, frictional damping starts to dominate. When the hydrodynamic screening length scale becomes much smaller than the active length scale, the energy available to create and sustain defects diminishes. Consequently, the system transitions to closely spaced walls that do not decay into defects, leading to a decrease in the number of defects at higher values of friction.

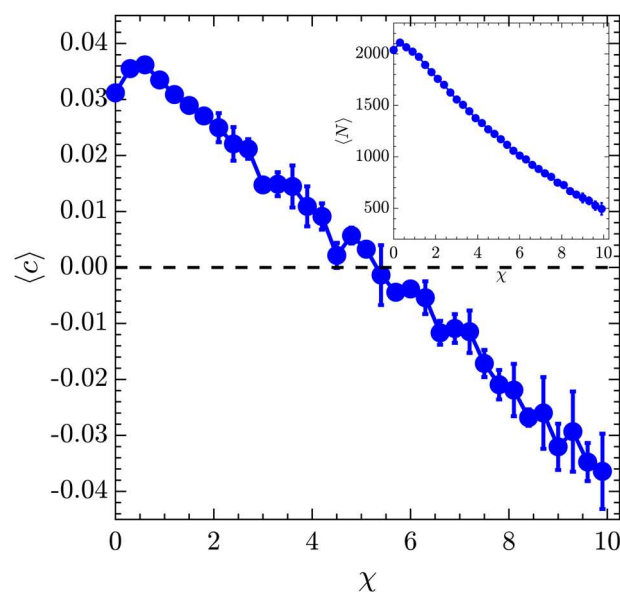


**Fig. 10 | Effect of isotropic friction coefficient,  $\chi$ .** The charge of the active fluid changes with increase in the isotropic friction coefficient for  $\zeta = 0.15$  and  $K = 0.05$ . Inset shows the variation of the number of defects with the strength of the isotropic friction. The error bars represent the standard deviation from three distinct simulations, each initialized with a unique random seed defining the random distribution of the director field,  $\mathbf{n}$ .

Additionally, the increase in friction reduces the velocity-velocity correlations<sup>59,60</sup>, affecting the efficacy of streak propagation and the merging process involving the  $+1/2$  defects (Fig. 5e, f). Moreover, strong friction reduces the mobility of  $+1/2$  defects in the passive fluid more than in the active fluid, causing the  $+1/2$  defects to localize in the passive fluid, thus resulting in a negatively charged active fluid. In summary, akin to the effect of anchoring strength and orientational elasticity, an increase in isotropic friction decreases the charge of the active fluid. This suggests that the impact of the model parameters on charge segregation aligns with their influence on the activity and number of topological defects.

**Effect of the active fluid's volume fraction on its charge**

Finally, we explore how the charge segregation is affected by different proportions of passive to active fluids. The volume fraction of the active fluid ( $\phi_a$ ) is determined by the initial value of the order parameter via  $\phi_a = \phi(t = 0)$ . As shown in Fig. 11, the charge of the active fluid exhibits a non-monotonic variation with the volume fraction of the active fluid. Specifically, the charge of the active fluid increases with an increase in  $\phi_a$  until  $\phi_a \approx 0.6$ , after which it decreases. Thus, the maximum charge of the active fluid is observed when there is a minimal difference in the volume fraction of active and passive fluids.

The charge of the active fluid is positive for  $\phi_a = 0.5$ , indicating that the fraction of  $+1/2$  defects in the active fluid is more than that of  $-1/2$  defects. When  $\phi_a < 0.5$ , the decrease in the amount of active fluid limits the formation of a continuous network, as depicted in Fig. 11b. Consequently, more  $+1/2$  defects move into the passive fluid compared to the case of  $\phi_a = 0.5$ , leading to a decrease in charge. Conversely, when  $\phi_a > 0.5$ , the higher amount of active fluid facilitates the easier formation of a continuous network, resulting in an increase in the charge of the active fluid. However, when  $\phi_a \rightarrow 0$ , the total number of defects decreases due to a decrease in the fraction of active fluid, making the charge zero, and when  $\phi_a \rightarrow 1$ , both  $+1/2$  and  $-1/2$  defects predominantly remain within the active fluid as shown in Fig. 11c, suppressing the charge segregation and decreasing the active fluid's charge. Thus, the mechanisms driving the decrease in active fluid charge for low- and high-volume fractions of the active fluid are distinct.

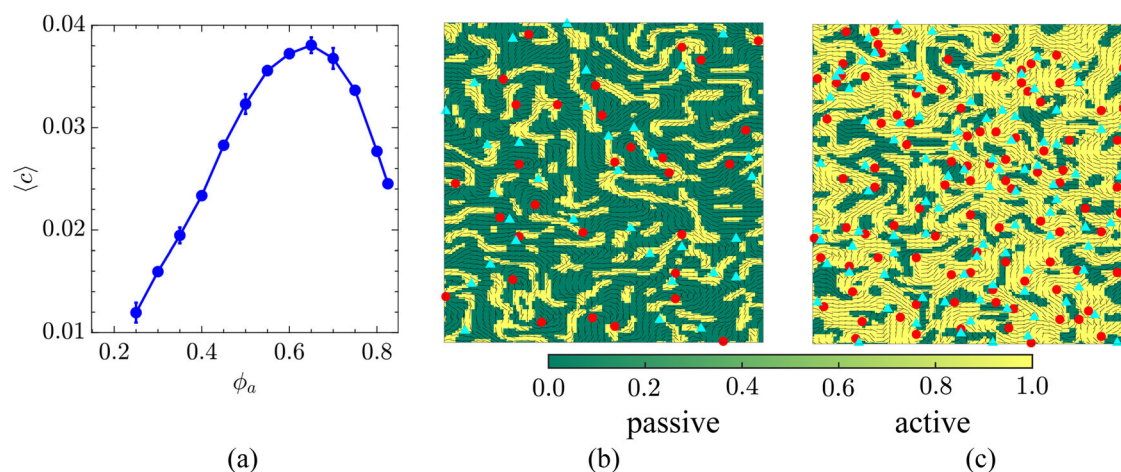


**Fig. 11 | Effect of active fluid's volume fraction.** **a** The variation in the charge of the active fluid with its volume fraction for  $\zeta = 0.15$  and  $K = 0.05$ . The error bars represent the standard deviation from three distinct simulations, each initialized with a unique random seed defining the random distribution of the director field,  $\mathbf{n}$ . The

instantaneous snapshot of the phase field variable ( $\phi$ ) with overlaid director field (black lines) and topological defects ( $+1/2$  depicted as red circles,  $-1/2$  defects as cyan triangles) for **(b)**  $\phi_a = 0.3$  and **(c)**  $\phi_a = 0.7$ .

## Conclusions and outlook

In this study, we investigated the dynamics of charge segregation and defect transport in a binary mixture of active-passive nematic fluids using a biphasic nematic framework. Our findings show that the phase separation of active and passive fluids is a dynamic process characterized by the continuous breaking and reforming of phase-separated domains.

While half-integer defects nucleate and annihilate in pairs, maintaining charge neutrality within the binary mixture, our results show that their uneven distribution between active and passive fluids can disrupt the charge balance within each fluid, leading to charge segregation. Previous studies<sup>19,26,44</sup> have noted a positively charged active nematic in dense cell colonies consisting of either one or two genotypes. In colonies with a single genotype, the accumulation of active species near  $+1/2$  defects is attributed to anisotropic friction<sup>26,44</sup>. This accumulation occurs due to the imbalance between the inflow and outflow of active species at the core of  $+1/2$  defects. However, charge segregation in biphasic mixtures composed of two genotypes does not necessitate anisotropic friction. Zhang et al.<sup>19</sup> observed that  $+1/2$  defects tend to migrate from the higher activity phase to the lower activity phase, resulting in the higher activity phase becoming negatively charged. Nevertheless, we demonstrated that charge segregation in a biphasic mixture relies on the interplay between interfacial tension and activity. Specifically, our findings suggest that the active fluid becomes positively charged when activity is high and interfacial tension is low. This happens because the  $+1/2$  defects primarily move within the active fluid due to the formation of a constantly reforming active fluid network, whereas the flow around  $-1/2$  defects tends to displace the active fluid. In contrast, when interfacial tension dominates over activity,  $+1/2$  defects migrate from the active fluid to the passive fluid, while  $-1/2$  defects tend to remain within its bulk, resulting in a negatively charged active fluid. Additionally, we examined the charge segregation in terms of active and capillary length scales.

Furthermore, we examined the impact of interfacial anchoring on charge segregation. The charge of the active fluid is found to decrease with increasing anchoring strength. This is attributed to the enhanced alignment of the director field with the interface, resulting in higher nematic order and fewer defects. This results in a decrease in the charge of the active fluid. Additionally, through analysis of the orientational elasticity and isotropic friction, we demonstrated that the impact of these model parameters on charge segregation aligns with their influence on activity and the number of topological defects. Moreover, we observed that the charge of the active fluid exhibits a non-monotonic variation with the volume fraction of active fluid, with distinct mechanisms driving charge segregation for low and high-

volume fractions. For a given concentration of the active fluid, charge segregation can be modulated by varying other model parameters. For instance, when the concentration of the active fluid exceeds that of the passive fluid, decreasing the anchoring strength increases the charge of the active fluid, indicating a higher concentration of  $+1/2$  defects in the active fluid (Supplementary Fig. 4). Given that  $+1/2$  defects are associated with compressive stress and  $-1/2$  defects with tensile stress<sup>10</sup>, these interactions may preferentially favor certain genotypes over others.

Several studies have explored the distinct roles of differential cell motility and adhesion in cell segregation<sup>61–65</sup>. According to the differential adhesion hypothesis<sup>66,67</sup>, cells sort into spatially distinct subpopulations to minimize their surface area, similar to interfacial tension in fluids<sup>39,40</sup>. Additionally, studies with avian and fish embryonic cells have shown that interfacial tension significantly impacts cell segregation<sup>42,68,69</sup>, with higher-adhesion cells clustering together and minimizing contact with cells of lower adhesion<sup>40</sup>. However, different cell types that encounter one another often display different levels of motility, which has also been implicated in cell sorting and pattern formation. Méhes et al.<sup>37</sup> found that in co-cultures of keratocyte types from different species, faster-moving cells demonstrated more correlated motion and directional persistence, efficiently segregating from slower-moving counterparts. Although they did not examine topological defects and nematic order, their observations align with our findings of an active fluid network when the activity is large and the active fluid follows the movement of  $+1/2$  topological defects.

Recent advancements in genetic engineering give experimentalists the ability to control motility and adhesion in mixed synthetic multicellular communities with an exquisite level of precision. For example, adhesion molecules can be engineered to tune the strength of adhesion between different cell types in mixtures of bacteria<sup>70</sup> and in mixtures of eukaryotes<sup>71</sup>, allowing the direct control of effective interfacial tension between different genotypes. Such approaches could be used to directly test our predictions on the role topological defects play in biphasic systems and ultimately shed light on tissue organization and pattern formation in natural multicellular communities. As motile and non-motile cells routinely encounter each other in natural environments and the human body<sup>72–76</sup>, our simulations lay the foundation for understanding the emergent physical processes that structure these microscale ecosystems, potentially leading to new ways to control them.

## Data availability

All data needed to evaluate the conclusions in the paper are present in the paper and the Supplementary Materials.

## Code availability

Code is available from the corresponding author upon polite request.

Received: 1 May 2024; Accepted: 28 August 2024;

Published online: 06 September 2024

## References

- Vlamakis, H., Aguilar, C., Losick, R. & Kolter, R. Control of cell fate by the formation of an architecturally complex bacterial community. *Genes Dev.* **22**, 945 (2008).
- Gude, S. et al. Bacterial coexistence driven by motility and spatial competition. *Nature* **578**, 588 (2020).
- Muok, A. & Briegel, A. Intermicrobial hitchhiking: how nonmotile microbes leverage communal motility. *Trends Microbiol.* **29**, 542 (2021).
- Xu, H., Dauparas, J., Das, D., Lauga, E. & Wu, Y. Self-organization of swimmers drives long-range fluid transport in bacterial colonies. *Nat. Commun.* **10**, 1792 (2019).
- Curatolo, A. et al. Cooperative pattern formation in multi-component bacterial systems through reciprocal motility regulation. *Nat. Phys.* **16**, 1152 (2020).
- Benisty, S., Ben-Jacob, E., Ariel, G. & Be'er, A. Antibiotic-induced anomalous statistics of collective bacterial swarming. *Phys. Rev. Lett.* **114**, 018105 (2015).
- Zuo, W. & Wu, Y. Dynamic motility selection drives population segregation in a bacterial swarm. *Proc. Nat. Acad. Sci.* **117**, 4693 (2020).
- Aktipis, C. A., Maley, C. C. & Pepper, J. W. Dispersal evolution in neoplasms: the role of dysregulated metabolism in the evolution of cell motility. *Cancer Prev. Res.* **5**, 266 (2012).
- Gallagher, J. A., Brown, J. S. & Anderson, A. R. The impact of proliferation-migration tradeoffs on phenotypic evolution in cancer. *Sci. Rep.* **9**, 2425 (2019).
- Saw, T. B., Xi, W., Ladoux, B. & Lim, C. T. Biological tissues as active nematic liquid crystals. *Adv. Mater.* **30**, 1802579 (2018).
- Armengol-Collado, J.-M., Carezza, L. N., Eckert, J., Krommydas, D. & Giomi, L. Epithelia are multiscale active liquid crystals. *Nat. Phys.* **19**, 1773 (2023).
- Dell'Arciprete, D. et al. A growing bacterial colony in two dimensions as an active nematic. *Nat. Commun.* **9**, 4190 (2018).
- Sanchez, T., Chen, D. T. N., DeCamp, S. J., Heymann, M. & Dogic, Z. Spontaneous motion in hierarchically assembled active matter. *Nature* **491**, 431 (2012).
- Zhang, R., Kumar, N., Ross, J. L., Gardel, M. L. & de Pablo, J. J. Interplay of structure, elasticity, and dynamics in actin-based nematic materials. *Proc. Natl Acad. Sci. USA.* **115**, E124 (2018).
- Doostmohammadi, A., Ignés-Mullol, J., Yeomans, J. M. & Sagués, F. Active nematics. *Nat. Commun.* **9**, 3246 (2018).
- Partovifard, A., Grawitter, J. & Stark, H. Controlling active turbulence by activity patterns. *Soft Matter* **20**, 1800 (2024).
- Mur, M., Kos, Ž., Ravnik, M. & Muševič, I. Continuous generation of topological defects in a passively driven nematic liquid crystal. *Nat. Commun.* **13**, 6855 (2022).
- Meacock, O. J., Doostmohammadi, A., Foster, K. R., Yeomans, J. M. & Durham, W. M. Bacteria solve the problem of crowding by moving slowly. *Nat. Phys.* **17**, 205 (2021).
- Zhang, D.-Q., Chen, P.-C., Li, Z.-Y., Zhang, R. & Li, B. Topological defect-mediated morphodynamics of active-active interfaces. *Proc. Natl Acad. Sci. USA.* **119**, e2122494119 (2022).
- Genkin, M. M., Sokolov, A., Lavrentovich, O. D. & Aranson, I. S. Topological defects in a living nematic ensnare swimming bacteria. *Phys. Rev. X* **7**, 011029 (2017).
- Sciortino, A. et al. Polarity and chirality control of an active fluid by passive nematic defects. *Nat. Mater.* **22**, 260 (2023).
- Zhang, R. et al. Spatiotemporal control of liquid crystal structure and dynamics through activity patterning. *Nat. Mat.* **20**, 875 (2021).
- Mozaffari, A., Zhang, R., Atzin, N. & De Pablo, J. J. Defect spirograph: Dynamical behavior of defects in spatially patterned active nematics. *Phys. Rev. Lett.* **126**, 227801 (2021).
- Shankar, S. & Marchetti, M. C. Hydrodynamics of active defects: From order to chaos to defect ordering. *Phys. Rev. X* **9**, 041047 (2019).
- Rønning, J., Marchetti, M. C. & Angheluta, L. Defect self-propulsion in active nematic films with spatially varying activity. *R. Soc. Open Sci.* **10**, 221229 (2023).
- Copenhagen, K., Alert, R., Wingreen, N. S. & Shaevitz, J. W. Topological defects promote layer formation in *Myxococcus xanthus* colonies. *Nat. Phys.* **17**, 211 (2021).
- Sonam, S. et al. Mechanical stress driven by rigidity sensing governs epithelial stability. *Nat. Phys.* **19**, 132 (2023).
- Bhattacharyya, S. & Yeomans, J. M. Phase separation driven by active flows. *Phys. Rev. Lett.* **130**, 238201 (2023).
- Caballero, F. & Marchetti, M. C. Activity-suppressed phase separation. *Phys. Rev. Lett.* **129**, 268002 (2022).
- Blow, M. L., Thampi, S. P. & Yeomans, J. M. Biphasic, lyotropic, active nematics. *Phys. Rev. Lett.* **113**, 248303 (2014).
- Adkins, R. et al. Dynamics of active liquid interfaces. *Science* **377**, 768 (2022).
- Coelho, R. C., Araújo, N. A. & da Gama, M. M. T. Active nematic-isotropic interfaces in channels. *Soft Matter* **15**, 6819 (2019).
- Coelho, R. C., Araújo, N. A. & da Gama, M. M. T. Propagation of active nematic-isotropic interfaces on substrates. *Soft Matter* **16**, 4256 (2020).
- Coelho, R. C., Figueiredo, H. R. & da Gama, M. M. T. Active nematics on flat surfaces: from droplet motility and scission to active wetting. *Phys. Rev. Res.* **5**, 033165 (2023).
- Saadaoui, M., Rocancourt, D., Roussel, J., Corson, F. & Gros, J. A tensile ring drives tissue flows to shape the gastrulating amniote embryo. *Science* **367**, 453 (2020).
- Yadav, V. et al. Gradients in solid surface tension drive marangoni-like motions in cell aggregates. *Phys. Rev. Fluids* **7**, L031101 (2022).
- Méhes, E., Mones, E., Nemeth, V. & Vicsek, T. Collective motion of cells mediates segregation and pattern formation in co-cultures. *PLoS One* **7**, e31711 (2012).
- McCandlish, S. R., Baskaran, A. & Hagan, M. F. Spontaneous segregation of self-propelled particles with different motilities. *Soft Matter* **8**, 2527 (2012).
- Foty, R. A., Forgacs, G., Pflieger, C. M. & Steinberg, M. S. Liquid properties of embryonic tissues: measurement of interfacial tensions. *Phys. Rev. Lett.* **72**, 2298 (1994).
- Foty, R. A., Pflieger, C. M., Forgacs, G. & Steinberg, M. S. Surface tensions of embryonic tissues predict their mutual envelopment behavior. *Development* **122**, 1611 (1996).
- Holtfreter, J. A study of the mechanics of gastrulation. *J. Exp. Zool.* **95**, 171 (1944).
- Schötz, E.-M. et al. Quantitative differences in tissue surface tension influence zebrafish germ layer positioning. *HFSP J.* **2**, 42 (2008).
- Manning, M. L., Foty, R. A., Steinberg, M. S. & Schoetz, E.-M. Coaction of intercellular adhesion and cortical tension specifies tissue surface tension. *Proc. Natl Acad. Sci. USA.* **107**, 12517 (2010).
- Kawaguchi, K., Kageyama, R. & Sano, M. Topological defects control collective dynamics in neural progenitor cell cultures. *Nature* **545**, 327 (2017).
- Mueller, R. & Doostmohammadi, A. Phase field models of active matter. Preprint at <https://arxiv.org/abs/2102.05557> (2021).
- Thampi, S. P., Golestanian, R. & Yeomans, J. M. Active nematic materials with substrate friction. *Phys. Rev. E* **90**, 062307 (2014).
- Marenduzzo, D., Orlandini, E., Cates, M. & Yeomans, J. Steady-state hydrodynamic instabilities of active liquid crystals: Hybrid lattice boltzmann simulations. *Phys. Rev. E* **76**, 031921 (2007).

48. Carena, L. N., Gonnella, G., Lamura, A., Negro, G. & Tiribocchi, A. Lattice boltzmann methods and active fluids. *Eur. Phys. J. E* **42**, 1 (2019).
49. Cahn, J. W. Phase separation by spinodal decomposition in isotropic systems. *J. Chem. Phys.* **42**, 93 (1965).
50. Datt, C., Thampi, S. P. & Govindarajan, R. Morphological evolution of domains in spinodal decomposition. *Phys. Rev. E* **91**, 010101 (2015).
51. Metselaar, L., Yeomans, J. M. & Doostmohammadi, A. Topology and morphology of self-deforming active shells. *Phys. Rev. Lett.* **123**, 208001 (2019).
52. Vafa, F. & Mahadevan, L. Active nematic defects and epithelial morphogenesis. *Phys. Rev. Lett.* **129**, 098102 (2022).
53. Bagnani, M., Azzari, P., De Michele, C., Arcari, M. & Mezzenga, R. Elastic constants of biological filamentous colloids: estimation and implications on nematic and cholesteric tactoid morphologies. *Soft Matter* **17**, 2158 (2021).
54. Giomi, L. & DeSimone, A. Spontaneous division and motility in active nematic droplets. *Phys. Rev. Lett.* **112**, 147802 (2014).
55. Alert, R. Fingering instability of active nematic droplets. *J. Phys. A Math. Theor.* **55**, 234009 (2022).
56. Doostmohammadi, A., Thampi, S. P. & Yeomans, J. M. Defect-mediated morphologies in growing cell colonies. *Phys. Rev. Lett.* **117**, 048102 (2016).
57. Vazquez, K., Saraswathibhatla, A. & Notbohm, J. Effect of substrate stiffness on friction in collective cell migration. *Sci. Rep.* **12**, 2474 (2022).
58. Schimming, C. D., Reichhardt, C. & Reichhardt, C. Friction-mediated phase transition in confined active nematics. *Phys. Rev. E* **108**, L012602 (2023).
59. Doostmohammadi, A., Adamer, M. F., Thampi, S. P. & Yeomans, J. M. Stabilization of active matter by flow-vortex lattices and defect ordering. *Nat. Commun.* **7**, 10557 (2016).
60. Rozman, J., Chaithanya, K. V. S., Yeomans, J. M. & Sknepnek, R. From dry to wet vertex model dynamics: Generating sustained flows. Preprint at <https://arxiv.org/abs/2312.11756> (2023).
61. Steinberg, M. S. Reconstruction of tissues by dissociated cells: some morphogenetic tissue movements and the sorting out of embryonic cells may have a common explanation. *Science* **141**, 401 (1963).
62. Rieu, J. P., Kataoka, N. & Sawada, Y. Quantitative analysis of cell motion during sorting in two-dimensional aggregates of dissociated hydra cells. *Phys. Rev. E* **57**, 924 (1998).
63. Duguay, D., Foty, R. A. & Steinberg, M. S. Cadherin-mediated cell adhesion and tissue segregation: qualitative and quantitative determinants. *Dev. Biol.* **253**, 309 (2003).
64. Cochet-Escartin, O., Locke, T. T., Shi, W. H., Steele, R. E. & Collins, E.-M. S. Physical mechanisms driving cell sorting in hydra. *Biophys. J.* **113**, 2827 (2017).
65. Méhes, E. et al. 3d cell segregation geometry and dynamics are governed by tissue surface tension regulation. *Commun. Biol.* **6**, 817 (2023).
66. Foty, R. A. & Steinberg, M. S. The differential adhesion hypothesis: a direct evaluation. *Dev. Biol.* **278**, 255 (2005).
67. Brodland, G. W. The differential interfacial tension hypothesis (dith): a comprehensive theory for the self-rearrangement of embryonic cells and tissues. *J. Biomech. Eng.* **124**, 188 (2002).
68. Townes, P. L. & Holtfreter, J. Directed movements and selective adhesion of embryonic amphibian cells. *J. Exp. Zool.* **128**, 53 (1955).
69. Nicol, A. & Garrod, D. The sorting out of embryonic cells in monolayer, the differential adhesion hypothesis and the non-specificity of cell adhesion. *J. Cell Sci.* **38**, 249 (1979).
70. Glass, D. S. & Riedel-Kruse, I. H. A synthetic bacterial cell-cell adhesion toolbox for programming multicellular morphologies and patterns. *Cell* **174**, 649 (2018).
71. Stevens, A. J. et al. Programming multicellular assembly with synthetic cell adhesion molecules. *Nature* **614**, 144 (2023).
72. Yang, H.-H., Vinopal, R. T., Grasso, D. & Smets, B. F. High diversity among environmental *Escherichia coli* isolates from a bovine feedlot. *Appl. Environ. Microbiol.* **70**, 1528 (2004).
73. Vos, M. & Velicer, G. J. Natural variation of gliding motility in a centimetre-scale population of *Myxococcus xanthus*. *FEMS Microbiol. Ecol.* **64**, 343 (2008).
74. Clark, S. T. et al. Phenotypic diversity within a *Pseudomonas aeruginosa* population infecting an adult with cystic fibrosis. *Sci. Rep.* **5**, 10932 (2015).
75. Kwon, T., Kwon, O.-S., Cha, H.-J. & Sung, B. J. Stochastic and heterogeneous cancer cell migration: experiment and theory. *Sci. Rep.* **9**, 16297 (2019).
76. Zanotelli, M. R. et al. Highly motile cells are metabolically responsive to collagen density. *Proc. Natl Acad. Sci. USA.* **119**, e2114672119 (2022).
77. Giomi, L., Bowick, M. J., Mishra, P., Sknepnek, R. & Cristina Marchetti, M. Defect dynamics in active nematics. *Philos. Trans. A Math. Phys. Eng. Sci.* **372**, 20130365 (2014).

## Acknowledgements

C.K.V.S. acknowledges the Post-Doctoral Equivalent Fellowship from the Indian Institute of Technology Madras for supporting this research. A.A. acknowledges support from the EU's Horizon Europe research and innovation program under the Marie Skłodowska-Curie grant agreement No. 101063870 (TopCellComm). W.M.D. acknowledges support from the Biotechnology and Biological Sciences Research Council New Investigator grant (BBSRC grant no. BB/R018383/1) and a Human Frontier Science Program grant (HFSP grant no. RGY0080/2021). A.D. acknowledges funding from the Novo Nordisk Foundation (grant No. NNF18SA0035142 and NERD grant No. NNF21OC0068687), Villum Fonden (Grant no. 29476), and the European Union (ERC, PhysCoMeT, 101041418). Views and opinions expressed are however those of the authors only and do not necessarily reflect those of the European Union or the European Research Council. Neither the European Union nor the granting authority can be held responsible for them.

## Author contributions

C.K.V.S., A.A., S.P.T., and A.D. designed and performed the research. C.K.V.S. wrote the first draft of the manuscript. C.K.V.S., A.A., O.J.M., W.M.D., S.P.T., and A.D. analyzed the results and contributed to editing the manuscript.

## Competing interests

A.D. is an Editorial Board Member for Communications Physics but was not involved in the editorial review of or the decision to publish this article. All the other authors declare no competing interests.

## Additional information

**Supplementary information** The online version contains supplementary material available at <https://doi.org/10.1038/s42005-024-01792-6>.

**Correspondence** and requests for materials should be addressed to Sumesh P. Thampi or Amin Doostmohammadi.

**Peer review information** *Communications Physics* thanks the anonymous reviewers for their contribution to the peer review of this work. A peer review file is available.

**Reprints and permissions information** is available at <http://www.nature.com/reprints>

**Publisher's note** Springer Nature remains neutral with regard to jurisdictional claims in published maps and institutional affiliations.

**Open Access** This article is licensed under a Creative Commons Attribution-NonCommercial-NoDerivatives 4.0 International License, which permits any non-commercial use, sharing, distribution and reproduction in any medium or format, as long as you give appropriate credit to the original author(s) and the source, provide a link to the Creative Commons licence, and indicate if you modified the licensed material. You do not have permission under this licence to share adapted material derived from this article or parts of it. The images or other third party material in this article are included in the article's Creative Commons licence, unless indicated otherwise in a credit line to the material. If material is not included in the article's Creative Commons licence and your intended use is not permitted by statutory regulation or exceeds the permitted use, you will need to obtain permission directly from the copyright holder. To view a copy of this licence, visit <http://creativecommons.org/licenses/by-nc-nd/4.0/>.

© The Author(s) 2024